Evidence of the fractional quantum spin Hall effect in moiré $MoTe_2$

https://doi.org/10.1038/s41586-024-07214-5

Received: 27 November 2023

Accepted: 20 February 2024

Published online: 20 March 2024

Check for updates

Kaifei Kang[1]✉, Bowen Shen[1], Yichen Qiu[2], Yihang Zeng[2], Zhengchao Xia[1], Kenji Watanabe[3], Takashi Taniguchi[3], Jie Shan[1,2,4]✉ & Kin Fai Mak[1,2,4]✉

Quantum spin Hall (QSH) insulators are two-dimensional electronic materials that have a bulk band gap similar to an ordinary insulator but have topologically protected pairs of edge modes of opposite chiralities[1–6]. So far, experimental studies have found only integer QSH insulators with counter-propagating up-spins and down-spins at each edge leading to a quantized conductance $G_0 = e^2/h$ (with e and h denoting the electron charge and Planck's constant, respectively)[7–14]. Here we report transport evidence of a fractional QSH insulator in 2.1° twisted bilayer $MoTe_2$, which supports spin-S_z conservation and flat spin-contrasting Chern bands[15,16]. At filling factor $\nu = 3$ of the moiré valence bands, each edge contributes a conductance $\frac{3}{2}G_0$ with zero anomalous Hall conductivity. The state is probably a time-reversal pair of the even-denominator 3/2-fractional Chern insulators. Furthermore, at $\nu = 2$, 4 and 6, we observe a single, double and triple QSH insulator with each edge contributing a conductance G_0, $2G_0$ and $3G_0$, respectively. Our results open up the possibility of realizing time-reversal symmetric non-abelian anyons and other unexpected topological phases in highly tunable moiré materials[17–19].

The emergence of two-dimensional moiré materials has introduced a platform for exploring quantum phases of matter that arise from electronic topology and correlations[17–20]. In particular, twisted transition metal dichalcogenides (TMDs) in the AA-stacking structure form a honeycomb moiré lattice with two sublattice sites residing in separate TMD layers[15,16,21]. The topmost moiré valence bands, originated from the K- and K′-valley states of the monolayer TMDs, are spin-split and spin-valley locked by a large Ising (out-of-plane) spin-orbit field, which defines the spin quantization axis[22]. The continuum model band structure calculations have shown that flat Chern bands with spin- and valley-contrasting Chern numbers emerge in small-angle twisted TMDs as a result of skyrmion-like interlayer hopping[15]. Both integer Chern insulator at moiré band filling factor $\nu = 1$ and fractional Chern insulators at $\nu = 3/5$ and 2/3 have been recently reported in twisted bilayer $MoTe_2$ ($tMoTe_2$) under zero magnetic field[23–26].

In this work, we study electrical transport in 2.1° $tMoTe_2$ with moiré density $n_M \approx 1.26 \times 10^{12}$ cm^{-2}. The smaller twist angle compared with the reported studies[23–26] (twist angle around 3.5° and moiré density around 3.5×10^{12} cm^{-2}) further flattens and isolates the Chern bands[15,16,27–35] and enables us to observe interaction effects at high filling factors ($\nu \geq 2$). By combining local and nonlocal transport with different measurement configurations, we observe, apart from the reported Chern insulator at $\nu = 1$, a QSH insulator with one, two and three pairs of helical edge modes, with each pair contributing a conductance G_0 at $\nu = 2$, 4 and 6, respectively (more than one pair is allowed because of spin-S_z conservation[36]). But most importantly, we observe evidence of a QSH insulator at $\nu = 3$ with each edge contributing a conductance $\frac{3}{2}G_0$, which can be explained only by charge fractionalization[4,37–41]. Charge fractionalization is of substantial interest to both fundamental physics and fault-tolerant topological quantum computing[42]. It has been observed in the fractional quantum Hall states in high-mobility two-dimensional (2D) electrons subjected to a high magnetic field[43] and in fractionally filled Hofstadter and Chern bands in moiré materials[23–26,44–46]. But unlike all known cases, in which time-reversal symmetry breaking (either explicitly or spontaneously) is essential, the fractional QSH insulator observed here is time-reversal invariant.

Device design and characterization

We use the dual-gated device structure (Fig. 1a), in which the top and bottom gates independently control the moiré band filling factor, ν, and the out-of-plane electric field, E. The latter tunes the interlayer or moiré sublattice potential difference[23–26]. To facilitate contact formation for hole transport in $tMoTe_2$, we use platinum (Pt) electrodes, contact gates to heavily hole-dope the $tMoTe_2$ regions adjacent to the metal electrodes and monolayer WSe_2 between Pt and $tMoTe_2$ as a tunnel barrier. In this design (Extended Data Fig. 1), a tunnel barrier occurs only at the metal-heavily doped $tMoTe_2$ junctions; the junctions between the $tMoTe_2$ contact and channel regions are nearly transparent (see below)—that is, the contact resistance arises nearly entirely from the metal junctions. We achieve contact resistances down to about 25 kΩ (per contact) at low temperatures and nearly independent of the channel filling factor down to $\nu < 1$. By contrast, it remains challenging to achieve uniform moiré devices at very small twist angles as in this study probably because of structural relaxation[19]. We choose to study a small region (about 2×5 μm^2) with relatively uniform moiré as shown in Fig. 1b. The region of interest (shaded in red) with four

[1]School of Applied and Engineering Physics, Cornell University, Ithaca, NY, USA. [2]Department of Physics, Cornell University, Ithaca, NY, USA. [3]National Institute for Materials Science, Tsukuba, Japan. [4]Kavli Institute at Cornell for Nanoscale Science, Ithaca, NY, USA. ✉e-mail: kk726@cornell.edu; jie.shan@cornell.edu; kinfai.mak@cornell.edu

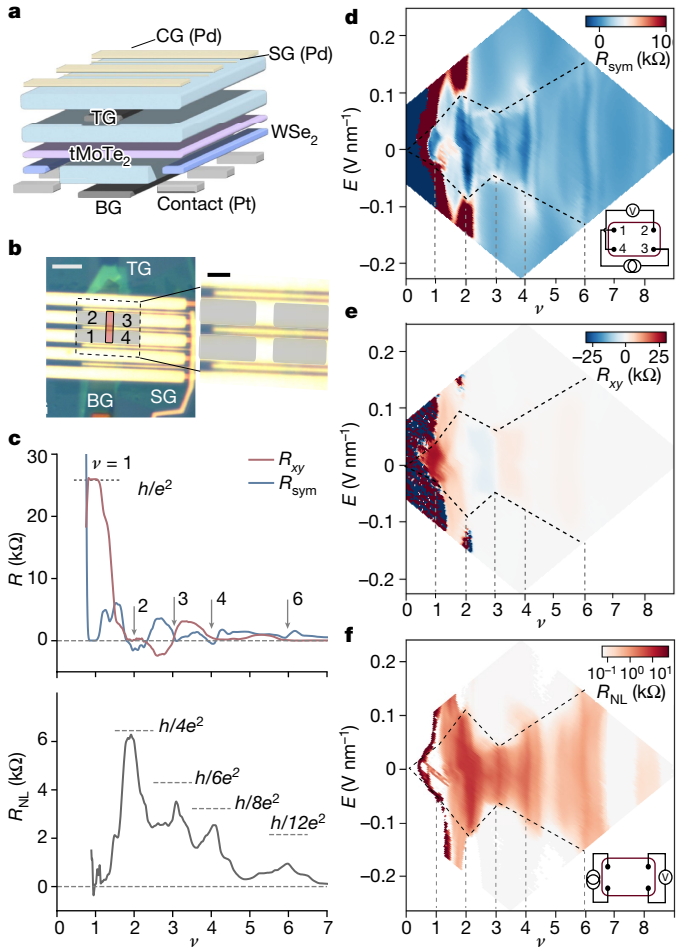

Fig. 1 | Moiré $MoTe_2$ device and characterization. a, Schematic of dual-gated $tMoTe_2$ devices. Both top gate (TG) and bottom gate (BG) are made of few-layer graphite contacts (dark grey) and hBN dielectrics (light blue). Monolayer WSe_2 (blue) is a tunnel barrier between the Pt contact electrodes (grey) and $tMoTe_2$ (purple). Palladium (yellow) is used as contact gates (CG) and split gates (SG). **b**, Optical micrograph of the 2.1° $tMoTe_2$ device with the region of interest shaded in red and four contact electrodes (1–4) shaded in grey. **c**, Line-cut of **d**–**f** at $E \approx 0$. The dashed lines denote the expected resistance around $\nu = 1, 2, 3, 4$ and 6. **d**–**f**, Four-terminal resistance R_{sym} (**d**), Hall resistance R_{xy} (**e**) and nonlocal resistance R_{NL} (**f**) versus vertical electric field E and filling factor ν at 20 mK. The measurement configurations for **d**, **e** and for **f** are shown in the inset of **d** and **f**, respectively. R_{sym} and R_{xy} are the field symmetric and anti-symmetric parts of the measured resistance at $B_\perp = \pm 0.1$ T; R_{NL} is measured under 0.1 T. The black dashed lines are guides to the eye of the layer-hybridized regime; the grey dashed lines denote filling factor $\nu = 1, 2, 3, 4$ and 6. Scale bars, 5 μm (**b**) and 2 μm (**b**, inset).

low resistance contacts (1–4, shaded in grey) has a twist angle of 2.1°. The other regions of the device do not show the moiré effects and are electrically disconnected from the region of interest. See the Methods for details on device fabrication, twist-angle calibration (Extended Data Fig. 2) and contact resistance characterization (Extended Data Fig. 1).

We perform electrical transport studies as described in the Methods. Unless otherwise specified, all measurements are at lattice temperature $T = 20$ mK. Figure 1d,e show the four-terminal resistances (R_{sym} and R_{xy}) of the device as a function of E and ν. Here R_{sym} and R_{xy} are the field symmetric and anti-symmetric parts of the resistance measured at small out-of-plane magnetic fields $B_\perp = \pm 0.1$ T using the configuration shown in Fig. 1d (inset). A line-cut of Fig. 1d,e along $E \approx 0$ is shown in Fig. 1c (top). At $\nu = 1$, we observe a quantized $R_{xy} = h/e^2$ accompanied by a vanishing R_{sym}. This is an integer Chern insulator, consistent with earlier studies on larger twist-angle $tMoTe_2$ (refs. 23–26). A fractional Chern insulator with a weak Hall plateau and an R_{sym} minimum is also observed near $\nu = 3/2$. In addition to the Chern insulators, we observe a series of states with nearly vanishing R_{sym} at integer fillings up to about $\nu = 8$ but nearly no Hall response (see Fig. 2a and inset for more evidence of $R_{xy} \approx 0$). We focus on the most prominent ones at $\nu = 2, 3, 4$ and 6. The nearly vanishing R_{xy} and R_{sym} suggest that these states are neither trivial band insulators nor Chern insulators.

The nature of these states changes abruptly above a certain electric field, E_c, which is marked schematically by the black dashed lines in Fig. 1d,e. Specifically, the states at $\nu = 1$ and 2 turn into highly insulating states for $E > E_c$, whereas those at $\nu = 3$, 4 and 6 become metallic; the Hall response is nearly absent irrespective of fillings for $E > E_c$. An electric-field-induced topological phase transition for the $\nu = 1$ Chern insulator has been demonstrated in larger twist-angle $tMoTe_2$ (refs. 23–26). The moiré bands in $tMoTe_2$ are topologically nontrivial only in the layer-hybridized regime for $E < E_c$ (refs. 15,16,33). The critical electric field E_c generally increases with filling because higher electric fields are required by electrostatics to polarize more charges to one layer. A similar electrostatics phase diagram has been observed in other TMD moiré bilayers[19,47].

We further characterize the nonlocal four-terminal resistance, R_{NL}, of the device as a function of E and ν in Fig. 1f using the measurement configuration shown in the inset. The nonlocal measurement is ensured by the length-to-width ratio (approximately 3) of the channel. A line cut along $E \approx 0$ is shown in Fig. 1c (bottom). We note that the device channel is highly symmetric; R_{NL} is nearly identical when the source–drain and voltage probe pairs are swapped (Extended Data Fig. 3). We observe a vanishing R_{NL} at $\nu = 1$, which is consistent with chiral edge transport associated with the Chern insulator. But R_{NL} exhibits prominent peaks at $\nu = 2$, 3, 4 and 6. Furthermore, large R_{NL} is present only in the layer-hybridized regime. It becomes negligible (about 10 Ω or less) compared with R_{sym} (about 2–5 kΩ) for $E > E_c$. All these results indicate edge-dominated transport at $\nu = 2$, 3, 4 and 6 in the layer-hybridized regime.

Integer and fractional QSH insulators

We perform comprehensive two-terminal resistance measurements (Figs. 2 and 3) to verify edge channel transport at $\nu = 2$, 3, 4 and 6 and to determine contribution per edge to conductance[8,10]. As discussed above, two-terminal resistance is the sum of resistances in series, including the channel resistance and contact resistance (Extended Data Fig. 1a). We calibrate the contact resistance for each measurement configuration as the difference between the two-terminal resistance and four-terminal resistance (R_{sym}) when the $tMoTe_2$ channel is heavily hole-doped and has a negligible $R_{sym} < 200$ Ω (Methods and Extended Data Fig. 1c). Two-terminal channel resistance, R_{2t}, is obtained by subtracting a constant (that is, ν- and E-independent) contact resistance from the measured resistance. Figure 2a shows the filling dependence of R_{2t} near $E = 0$ for the measurement configuration shown in Fig. 2b (inset). Figure 2b shows the corresponding two-terminal conductance, $G_{2t} = 1/R_{2t}$. A small magnetic field $B_\perp = 0.3$ T is applied to fully polarize the $\nu = 1$ Chern insulator (Fig. 2a, inset) but has a negligible effect on R_{2t} or G_{2t} (Extended Data Fig. 7). The quantized $R_{2t} = h/e^2$ or $G_{2t} = G_0$ plateau for the $\nu = 1$ Chern insulator state validates our procedure of contact resistance calibration.

Similar to the Chern insulator at $\nu = 1$, we observe nearly quantized plateaus of $R_{2t} = h/(\nu e^2)$ or $G_{2t} = \nu G_0$ around $\nu = 2$, 3, 4 and 6 (Fig. 2). The conductance plateaus are electric-field independent for small fields ($E < E_c$), whereas conductance in the compressible regions between two integer fillings is sensitive to E (Fig. 2b). The electric-field dependence of G_{2t} is shown in Fig. 3b–d for $\nu = 2$, 3 and 4 and Extended Data Fig. 4 for $\nu = 1$ and 6. We also include the result for three other

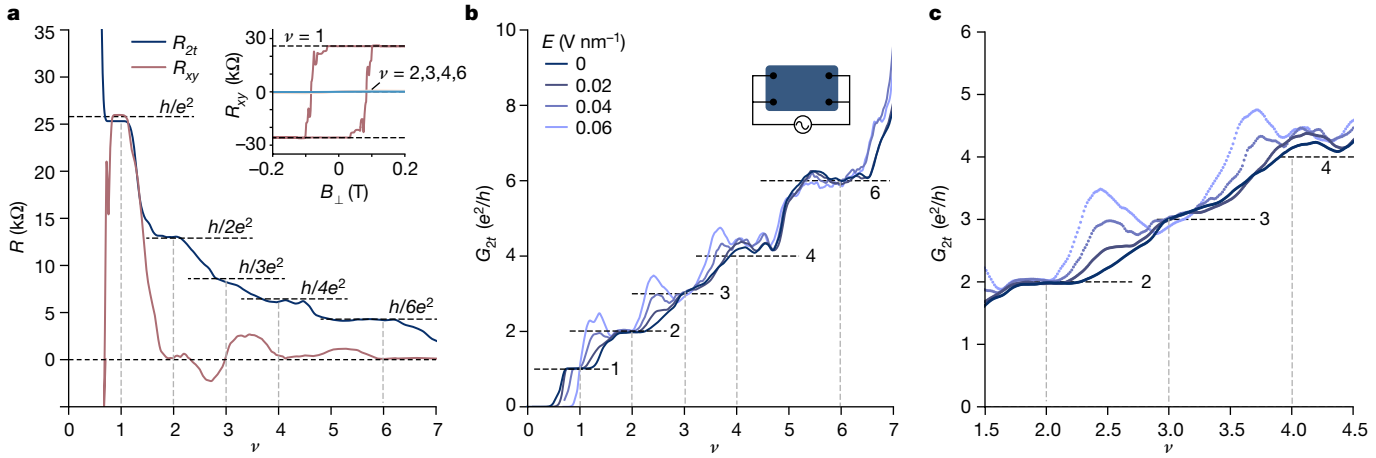

Fig. 2 | Quantized two-terminal transport. a, Filling factor dependence of two-terminal resistance (R_{2t}) and Hall resistance (R_{xy}) at $E \approx 0$ and 20 mK. Inset, R_{xy} shows a magnetic hysteresis and a quantized Hall resistance h/e^2 at zero magnetic field for $\nu = 1$; the Hall resistance is nearly zero for $\nu = 2, 3, 4$ and 6. **b**,**c**, Filling factor dependence of two-terminal conductance, $G_{2t} = 1/R_{2t}$ (in units of e^2/h), at representative electric fields in the layer-hybridized regime. The two-terminal measurement configuration is shown in the inset of **b**. A constant contact resistance 26.8 kΩ is subtracted from the measured two-terminal resistance to obtain R_{2t} (see the Methods for details). Magnetic field $B_\perp = 0.3$ T is applied to fully polarize the $\nu = 1$ Chern insulator state. The horizontal dashed lines are the expected resistance or conductance around $\nu = 1, 2, 3, 4$ and 6 (vertical dashed lines).

measurement configurations. The colour of the lines matches the colour of the channel in the measurement schematics in Fig. 3a. An electric-field plateau is observed in all cases, and the electric-field span of the conductance plateaus agrees well with the layer-hybridized regime (between the arrows) identified in Fig. 1. Furthermore, the value of the conductance plateaus is dependent on the measurement configuration for $\nu = 2, 3, 4$ and 6 (also see Extended Data Fig. 4). It closely matches ν, $\frac{3}{4}\nu$, $\frac{2}{3}\nu$ and $\frac{1}{2}\nu$ (in units of G_0), respectively, for the configurations from left to right in Fig. 3a. By contrast, the bulk conductance for the orange configuration in the layer-polarized region is higher than that for the light blue configuration (opposite to the behaviour in the layer-hybridized region); the conductance plateau $G_{2t} \approx G_0$ at $\nu = 1$ is also nearly independent of measurement configuration, which is consistent with chiral edge channel transport[10].

The transport behaviour observed at $\nu = 2, 3, 4$ and 6 can be fully described as helical edge transport within the Landauer–Büttiker formalism (Methods). The helical edge states are equilibrated at each contact and are populated according to the chemical potential of the contact from which they emanate[8,10]. This leads to a quantized resistance per edge (that is, the edge between two adjacent contacts). We can compute R_{2t} or G_{2t} for each measurement configuration using the equivalent circuit in Fig. 3a. The quantized resistance or conductance per edge is $2h/(\nu e^2)$ or $(1/2)\nu G_0$ to describe the results in Figs. 2 and 3 (dashed lines). Helical edge transport also explains the observed R_{sym}, R_{xy} and R_{NL} at $\nu = 2, 3, 4$ and 6 in Fig. 1c. First, the measurement configuration for the four-terminal resistance in Fig. 1d is effectively a bridge circuit, which gives a nearly vanishing R_{sym} (whereas R_{sym} for bulk transport does not vanish). (The remnant R_{sym}, especially at $\nu = 2$, is probably caused by the presence of backscattering in some of the edge channels in the bridge circuit, leading to a non-perfect cancellation in R_{sym}). Second, unlike Chern and quantum Hall insulators, the anomalous Hall response is absent because there is no net chirality. Third, the four-terminal nonlocal configuration in Fig. 1f gives $R_{NL} = \frac{1}{2\nu}\frac{h}{e^2}$ (dashed lines in Fig. 1c) by counting the number of edges involved.

All the results support that the $\nu = 2, 3, 4$ and 6 states are incompressible QSH insulators in the layer-hybridized regime (see Extended Data Fig. 8 for compressibility measurements). Specifically, for even filling factor $\nu = 2, 4$ and 6, each edge contributes a conductance G_0, $2G_0$ and $3G_0$, respectively. These states are consistent with integer QSH insulators with one, two and three pairs of helical edge modes, respectively, with each pair contributing a conductance G_0. For odd filling factor $\nu = 3$, each edge contributes a conductance $\frac{3}{2}G_0$, which can be explained only by charge fractionalization; the $\nu = 3$ state is consistent with a fractional QSH insulator[4,37–41].

Temperature dependence

We examine the energy scales of the QSH states by studying their temperature dependence. Figure 4a shows the filling factor dependence of G_{2t} near $E = 0$ with the same measurement configuration as in Fig. 2. The curves correspond to different temperatures ranging from 20 mK to 12 K and are vertically displaced for clarity. The contact resistance is calibrated at each temperature (Extended Data Fig. 1d). As temperature increases, the conductance plateaus are gradually smeared out, and at high temperatures the conductance smoothly increases with the filling factor. Specifically, the QSH plateaus at $\nu = 3$, 4 and 6 are smeared out above approximately 4 K, 10 K and 6 K, respectively; the $\nu = 2$ QSH plateau remains visible above 12 K (as a reference, the temperature of the Chern insulator at $\nu = 1$ is about 6 K). We estimate the gap size for the fractional QSH insulator to be about 0.3 meV. Similar energy scales are observed from the temperature dependence of four-terminal R_{NL} (Extended Data Fig. 5) and from compressibility measurements (Extended Data Fig. 8).

Figure 4b shows the electric-field dependence of G_{2t} for the fractional QSH insulator at varying temperatures (more data for the $\nu = 1, 2$ and 4 states are included in Extended Data Fig. 5). The conductance is weakly temperature dependent in the layer-hybridized regime with $E < E_c$; in the layer-polarized regime with $E > E_c$, G_{2t} decreases with increasing temperature, which is characteristic of a metal. The result suggests an electric-field-induced transition from a fractional QSH insulator to a Fermi liquid. Future studies based on Corbino geometry devices, which can access bulk transport in the fractional QSH insulator, are warranted to quantitatively study the quantum phase transition.

Discussions and conclusions

The observation of integer QSH insulators with a staircase-like dependence (Figs. 2 and 4) for the one, two and three pairs of helical edge states at $\nu = 2$, 4 and 6, respectively, shows the presence of several Landau-level-like Chern bands in 2.1° $tMoTe_2$. Our result is compatible with the first three moiré bands having Chern number +1 for the

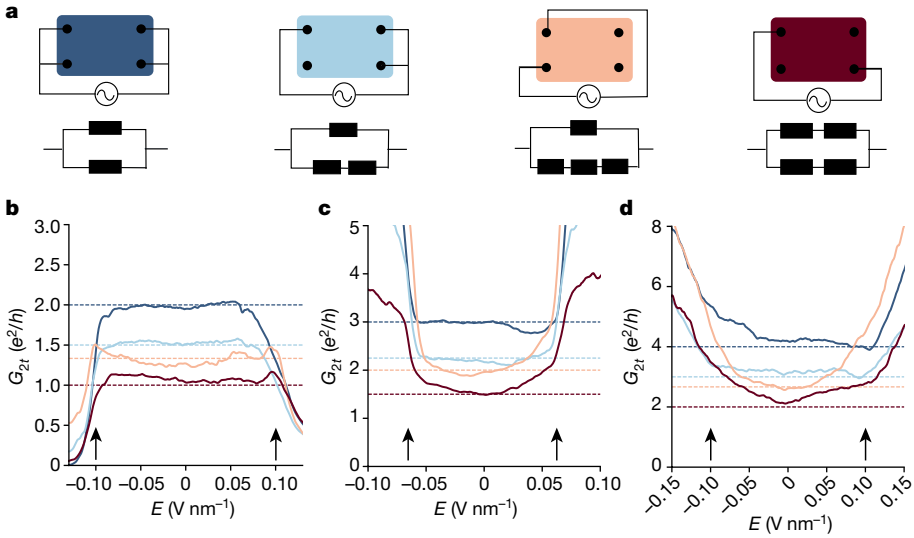

Fig. 3 | Two-terminal nonlocal transport. a, Four 2-terminal nonlocal measurement configurations (top) and equivalent circuits for helical edge mode transport (bottom). The shaded rectangles represent $tMoTe_2$ with four contacts (black dots). Unconnected dots are floated contacts. The equivalent resistor associated with helical edge transport is $2h/(\nu e^2)$ per edge for $\nu = 2$, 3 and 4. **b**–**d**, Electric-field dependence of G_{2t} (in units of e^2/h) for different measurement configurations around $\nu = 2$ (**b**), 3 (**c**) and 4 (**d**) at 20 mK. The horizontal dashed lines denote the expected conductance ν, $\frac{3}{4}\nu$, $\frac{2}{3}\nu$ and $\frac{1}{2}\nu$ in descending order from the Landauer–Büttiker analysis. The colour of the lines matches the colour of the channels in **a**. The layer-hybridized regime is between the two arrows for each filling factor.

K valley and Chern number −1 for the K′ valley (so that the number of helical edge state pairs adds up with increasing ν). This sequence of Chern bands is not fully consistent with the existing band structure calculations[15,16,27–33,35], which highlights the importance of electron interactions in modifying both the band dispersion and topology. An even number of helical edge state pairs is allowed here because they are protected by the spin-S_z conservation symmetry[22,36]. The Ising-like spin alignment of the helical edge states is supported by the experimental observation of anisotropic magneto-transport in Extended Data Fig. 7. Whereas G_{2t} is nearly independent of $B_\perp$ at $\nu = 2$, 3, 4 and 6, it decreases with in-plane magnetic field $B_\parallel$, which can induce spin mixing and backscattering[11–13].

The QSH insulator at $\nu = 3$ is of interaction origin; it occurs only in very small-angle $tMoTe_2$ (Extended Data Fig. 6). The observed zero Hall conductivity excludes the possibility of the state being a $\nu = 2$ QSH insulator plus a $\nu = 1$ valley-polarized Chern insulator. The incompressibility at $\nu = 3$ also excludes the possibility of a van Hove singularity and/or electron–hole compensation as the origin of the observed sign change in Hall response. The measured conductance, $\frac{3}{2}G_0$ per edge, can be explained only by charge fractionalization[4,37–41]. Furthermore, the spin-S_z conservation suggests that the state could be composed of two time-reversal copies of the spin-polarized even-denominator-3/2 fractional Chern insulator. This assignment is compatible with the sequence of spin–valley-contrasting Chern bands with negligible spin–valley mixing proposed above. However, we cannot exclude at this point other exotic forms of fractional QSH insulators with subtler time-reversal symmetry breaking, such as antiferromagnetic ordering, which could also give rise to similar experimental observations.

The observation of a fractional QSH insulator at $\nu = 3$ in $tMoTe_2$ leaves many open questions, such as the stability and the nature of

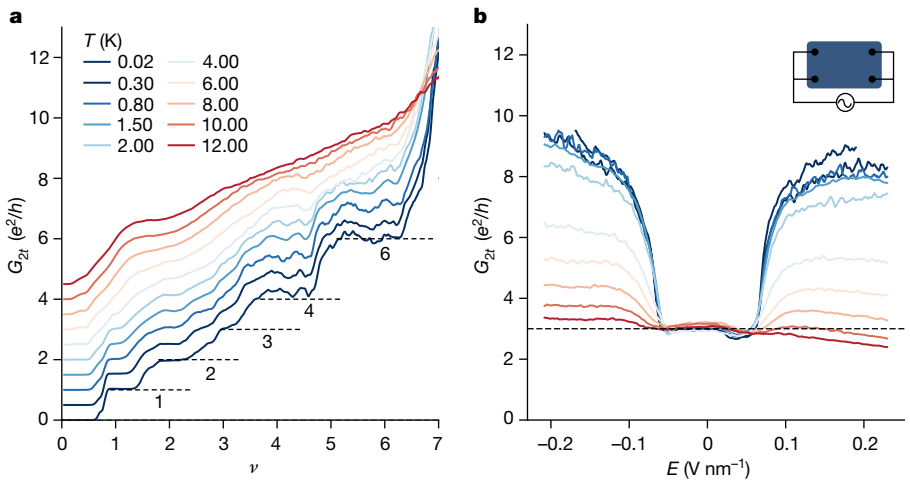

Fig. 4 | Topological phase transition and thermal excitations. a, Filling factor dependence of G_{2t} (in units of e^2/h, measured with the configuration in the inset of **b** at $E \approx 0$ and temperature ranging from 0.02 K to 12 K. The curves at different temperatures are vertically displaced by 0.5 units for clarity. **b**, Electric-field dependence of G_{2t} at $\nu = 3$ and varying temperatures. A QSH insulator-to-metal transition is observed with increasing electric field at critical field $E_c \approx \pm 70$ mV nm^{-1}. The horizontal dashed lines in **a**,**b** denote the expected conductance $\nu(e^2/h)$ around $\nu = 1, 2, 3, 4$ and 6. Magnetic field $B_\perp = 0.3$ T is applied to fully polarize the $\nu = 1$ Chern insulator.

the state. The fractional quantum Hall (FQH) state at 3/2 filling of the spin–valley-polarized Landau levels has been observed in monolayer TMD under high magnetic fields[48]; and the 3/2-FQH state is more robust than the odd-denominator 4/3- and 5/3-FQH states. Moreover, insulating states at integer filling factors are generally more robust than those at fractional fillings in moiré materials[19]. These points may shed light on the stability of the $\nu = 3$ fractional QSH state. Regarding the nature of the state, there are at least six possible candidates for the 3/2 fractional Chern insulator[37]: the Pfaffian state, the 331 state, the strong-pairing state and their particle–hole conjugates. In the absence of spin–valley mixing, the 3/2 fractional Chern insulator is similar to the single-component 3/2-FQH state in monolayer TMDs[48]; the Pfaffian or anti-Pfaffian state, which can support non-abelian excitations, is probably the stable ground state. Future experimental and theoretical studies are required to fully understand the nature of this exotic state and its competition with other symmetry-breaking phases.

Online content

Any methods, additional references, Nature Portfolio reporting summaries, source data, extended data, supplementary information, acknowledgements, peer review information; details of author contributions and competing interests; and statements of data and code availability are available at https://doi.org/10.1038/s41586-024-07214-5.

1. Kane, C. L. & Mele, E. J. Quantum spin Hall effect in graphene. *Phys. Rev. Lett.* **95**, 226801 (2005).
2. Kane, C. L. & Mele, E. J. Z_2 topological order and the quantum spin Hall effect. *Phys. Rev. Lett.* **95**, 146802 (2005).
3. Bernevig, B. A., Hughes, T. L. & Zhang, S. C. Quantum spin Hall effect and topological phase transition in HgTe quantum wells. *Science* **314**, 1757–1761 (2006).
4. Bernevig, B. A. & Zhang, S.-C. Quantum spin Hall effect. *Phys. Rev. Lett.* **96**, 106802 (2006).
5. Sheng, D. N., Weng, Z. Y., Sheng, L. & Haldane, F. D. M. Quantum spin-Hall effect and topologically invariant Chern numbers. *Phys. Rev. Lett.* **97**, 036808 (2006).
6. Hasan, M. Z. & Kane, C. L. *Colloquium:* topological insulators. *Rev. Mod. Phys.* **82**, 3045–3067 (2010).
7. Konig, M. et al. Quantum spin hall insulator state in HgTe quantum wells. *Science* **318**, 766–770 (2007).
8. Roth, A. et al. Nonlocal transport in the quantum spin Hall state. *Science* **325**, 294–297 (2009).
9. Knez, I., Du, R. R. & Sullivan, G. Evidence for helical edge modes in inverted InAs/GaSb quantum wells. *Phys. Rev. Lett.* **107**, 136603 (2011).
10. Young, A. F. et al. Tunable symmetry breaking and helical edge transport in a graphene quantum spin Hall state. *Nature* **505**, 528–532 (2014).
11. Fei, Z. et al. Edge conduction in monolayer WTe_2. *Nat. Phys.* **13**, 677–682 (2017).
12. Wu, S. F. et al. Observation of the quantum spin Hall effect up to 100 kelvin in a monolayer crystal. *Science* **359**, 76–79 (2018).
13. Li, T. et al. Quantum anomalous Hall effect from intertwined moiré bands. *Nature* **600**, 641–646 (2021).
14. Zhao, W. et al. Realization of the Haldane Chern insulator in a moiré lattice. *Nat. Phys.* **20**, 275–280 (2024).
15. Wu, F. C., Lovorn, T., Tutuc, E., Martin, I. & MacDonald, A. H. Topological insulators in twisted transition metal dichalcogenide homobilayers. *Phys. Rev. Lett.* **122**, 086402 (2019).
16. Devakul, T., Crepel, V., Zhang, Y. & Fu, L. Magic in twisted transition metal dichalcogenide bilayers. *Nat. Commun.* **12**, 6730 (2021).
17. Andrei, E. Y. et al. The marvels of moiré materials. *Nat. Rev. Mater.* **6**, 201–206 (2021).
18. Kennes, D. M. et al. Moire heterostructures as a condensed-matter quantum simulator. *Nat. Phys.* **17**, 155–163 (2021).
19. Mak, K. F. & Shan, J. Semiconductor moire materials. *Nat. Nanotechnol.* **17**, 686–695 (2022).
20. Cao, Y. et al. Unconventional superconductivity in magic-angle graphene superlattices. *Nature* **556**, 43–50 (2018).
21. Wang, L. et al. Correlated electronic phases in twisted bilayer transition metal dichalcogenides. *Nat. Mater.* **19**, 861–866 (2020).
22. Xiao, D., Liu, G. B., Feng, W., Xu, X. & Yao, W. Coupled spin and valley physics in monolayers of MoS_2 and other group-VI dichalcogenides. *Phys. Rev. Lett.* **108**, 196802 (2012).
23. Cai, J. et al. Signatures of fractional quantum anomalous Hall states in twisted $MoTe_2$. *Nature* **622**, 63–68 (2023).
24. Zeng, Y. et al. Thermodynamic evidence of fractional Chern insulator in moire $MoTe_2$. *Nature* **622**, 69–73 (2023).
25. Park, H. et al. Observation of fractionally quantized anomalous Hall effect. *Nature* **622**, 74–79 (2023).
26. Xu, F. et al. Observation of Integer and Fractional Quantum Anomalous Hall Effects in Twisted Bilayer $MoTe_2$. *Phys. Rev.* **13**, 031037 (2023).
27. Reddy, A. P., Alsallom, F. F., Zhang, Y., Devakul, T. & Fu, L. Fractional quantum anomalous Hall states in twisted bilayer $MoTe_2$ and WSe_2. *Phys. Rev. B* **108**, 085117 (2023).
28. Wang, C. et al. Fractional Chern insulator in twisted bilayer $MoTe_2$. *Phys. Rev. Lett.* **132**, 036501 (2024).
29. Morales-Durán, N., Wei, N., Shi, J. & MacDonald, A. H. Magic angles and fractional Chern insulators in twisted homobilayer TMDs. Preprint at arxiv.org/abs/2308.03143 (2023).
30. Mao, N. et al. Lattice relaxation, electronic structure and continuum model for twisted bilayer $MoTe_2$. Preprint at arxiv.org/abs/2311.07533 (2023).
31. Crépel, V., Regnault, N. & Queiroz, R. The chiral limits of moiré semiconductors: origin of flat bands and topology in twisted transition metal dichalcogenides homobilayers. Preprint at https://arxiv.org/abs/2305.10477 (2023).
32. Jia, Y. et al. Moiré fractional Chern insulators I: first-principles calculations and continuum models of twisted bilayer $MoTe_2$. Preprint at arxiv.org/abs/2311.04958 (2023).
33. Li, B., Qiu, X-W, Wu, F. Electrically tuned topology and magnetism in twisted bilayer $MoTe_2$ at ν_h=1. *Phys. Rev. B* **109**, L041106 (2024).
34. Mai, P., Feldman, B. E. & Phillips, P. W. Topological Mott insulator at quarter filling in the interacting Haldane model. *Phys. Rev. Res.* **5**, 013162 (2023).
35. Morales-Durán, N. et al. Pressure-enhanced fractional Chern insulators along a magic line in moiré transition metal dichalcogenides. *Phys. Rev. Research* **5**, L032022 (2023).
36. Bai, Y. X. et al. Doubled quantum spin Hall effect with high-spin Chern number in α-antimonene and α-bismuthene. *Phys. Rev. B* **105**, 195142 (2022).
37. Levin, M. & Stern, A. Fractional topological insulators. *Phys. Rev. Lett.* **103**, 196803 (2009).
38. Maciejko, J. & Fiete, G. A. Fractionalized topological insulators. *Nat. Phys.* **11**, 385–388 (2015).
39. Neupert, T., Chamon, C., Iadecola, T., Santos, L. H. & Mudry, C. Fractional (Chern and topological) insulators. *Phys. Scr.* **2015**, 014005 (2015).
40. Stern, A. Fractional topological insulators: a pedagogical review. *Annu. Rev. Condens. Matter Phys.* **7**, 349–368 (2016).
41. Wu, Y.-M., Shaffer, D., Wu, Z. & Santos, L. H. Time-reversal invariant topological moiré flatband: a platform for the fractional quantum spin Hall effect. Preprint at https://arxiv.org/abs/2309.07222 (2023).
42. Nayak, C., Simon, S. H., Stern, A., Freedman, M. & Das Sarma, S. Non-Abelian anyons and topological quantum computation. *Rev. Mod. Phys.* **80**, 1083–1159 (2008).
43. Stormer, H. L., Tsui, D. C. & Gossard, A. C. The fractional quantum Hall effect. *Rev. Mod. Phys.* **71**, S298–S305 (1999).
44. Spanton, E. M. et al. Observation of fractional Chern insulators in a van der Waals heterostructure. *Science* **360**, 62–66 (2018).
45. Xie, Y. et al. Fractional Chern insulators in magic-angle twisted bilayer graphene. *Nature* **600**, 439–443 (2021).
46. Lu, Z. et al. Fractional quantum anomalous Hall effect in multilayer graphene. *Nature* **626**, 759–764 (2024).
47. Xu, Y. et al. A tunable bilayer Hubbard model in twisted WSe_2. *Nat. Nanotechnol.* **17**, 934–939 (2022).
48. Shi, Q. et al. Odd- and even-denominator fractional quantum Hall states in monolayer WSe_2. *Nat. Nanotechnol.* **15**, 569–573 (2020).

Methods

Device fabrication

Dual-gated devices of $tMoTe_2$ were fabricated using the tear-and-stack and layer-by-layer transfer method[49,50]. Figure 1a shows the device schematic. In short, flakes of monolayer $MoTe_2$, monolayer WSe_2, hexagonal boron nitride (hBN) and few-layer graphite were first exfoliated from bulk crystals onto Si/SiO_2 substrates and identified by their optical contrast. They were picked up using a polycarbonate thin film on PDMS (polydimethylsiloxane) in the following sequence: hBN, top gate graphite, top gate hBN, part of the $MoTe_2$ monolayer, the rest of the $MoTe_2$ monolayer with a small twist angle, two WSe_2 monolayers as the tunnel barrier for the contacts, bottom gate hBN and bottom gate graphite. The finished stack was released onto a Si/SiO_2 substrate with pre-patterned Pt electrodes in the Hall bar geometry at a temperature of 180 °C. The device channel is defined by the top gate graphite electrode. The contact and split gates were defined by standard electron beam lithography and evaporation of palladium. The split gate turns off the $tMoTe_2$ regions that are covered only by the bottom gate so that they do not contribute to transport. The $tMoTe_2$ channel is connected to the Pt electrodes through heavily hole-doped $tMoTe_2$ contact regions, which are controlled by the contact gates, to achieve low contact resistance (Extended Data Fig. 1a). The device was annealed at 200 °C under high vacuum ($<10^{-5}$ mbar) for 6 h to improve the contacts further.

An optical micrograph of the device is shown in Fig. 1b. The width of the metal contacts is 2 μm. The channel width defined by the separation between electrodes 2 and 3 (or 1 and 4) is 1.5 μm. The channel length is about 5 μm. The channel (with four contacts) is disconnected from the rest of the sample. We have examined two transport devices of different twist angles in this study (Extended Data Fig. 6). Two more devices with twist angles near 2.2° and 2.7° degrees were also examined by compressibility measurements (Extended Data Fig. 8). Details of the device geometry and compressibility measurements have been reported in refs. 24,51.

Electrical measurements

Electrical transport measurements were performed in a Bluefors LD250 dilution refrigerator equipped with a 12-T superconducting magnet. Low-frequency (11.77 Hz) lock-in techniques were used to measure the sample resistance under a constant bias voltage (0.3 mV), which excites a bias current of less than 10 nA to avoid sample heating and/or high bias effects. Voltage pre-amplifiers with large input impedance (100 MΩ) were used in the four-terminal resistance measurements.

Twist-angle calibration

We calibrated the twist angle of $MoTe_2$ moiré based on the Landau levels originating from $\nu = 2$ under high magnetic fields (Extended Data Fig. 2). Landau levels with index $\nu_{LL} = 1, 2$ and 3 are identified from nearly quantized R_{xy} and R_{sym} minimum. They are consistent with Landau levels being fully spin- and valley-polarized[48], for which the density difference between two successive Landau levels is $B_\perp/\Phi_0$, where $\Phi_0 = h/e$ denotes the magnetic flux quantum. We determine the moiré density n_M based on the known moiré filling factor ν. Using the moiré density, we determine the twist angle $\theta = a\sqrt{\frac{\sqrt{3}}{2}n_M}$, where $a \approx 3.5$ Å is the $MoTe_2$ lattice constant. Extended Data Fig. 2d shows the twist angle calibrated at different magnetic fields between 9 T and 11 T. It is independent of the field. The mean is 2.10° with an uncertainty of about ±0.05°. The corresponding moiré density is $n_M \approx 1.26 \times 10^{12}$ cm^{-2}.

Contact resistance characterization

Extended Data Fig. 1a shows a schematic of the electrical contacts to the device channel. The metal (Pt) electrodes are connected to the $tMoTe_2$ channel through a region of heavily hole-doped $tMoTe_2$. A tunnel barrier occurs at the metal-to-heavily doped $tMoTe_2$ junctions, but the junctions between the heavily doped $tMoTe_2$ contact and the lightly doped $tMoTe_2$ channel regions are nearly transparent (as evidenced by the quantized R_{2t} and R_{xy} in Fig. 2a; ref. 52). The contact resistance arises nearly entirely from the metal junctions. The two-terminal resistance is the sum of resistances in series, including the channel resistance and the two contact resistances[53].

Extended Data Fig. 1b shows the contact characterization for the two-terminal configuration shown in the inset. The results for the other two-terminal configurations are similar. The raw two-terminal resistance R_{2t} (measured near $E \approx 0$ at 20 mK) decreases with increasing filling factor. The different curves are for different contact gate voltages. They are nearly identical for the filling factor down to $\nu < 1$ except for a constant resistance offset; a more negative contact gate voltage corresponds to a smaller R_{2t}. This is consistent with filling independent contact resistances, the value of which is controlled only by the doping density in the contact region. A more negative contact gate voltage increases the hole doping density in the contact region and decreases the contact resistance. The result is fully consistent with the contact design in Extended Data Fig. 1a.

To calibrate the value of the contact resistance, we compare the raw two-terminal resistance with the four-terminal resistance R_{sym} under the same conditions when the channel is heavily doped (Extended Data Fig. 1c). The four-terminal resistance is below 200 Ω for $\nu > 10$, and the value is nearly temperature independent (inset). We subtract a constant resistance (the contact resistance) from the raw two-terminal resistance to match R_{sym} at large ν. Figure 2a shows R_{2t} for the measurement configuration given in Fig. 2b (inset) after subtraction of 26.8 kΩ. It shows $R_{2t} \approx h/e^2$ at $\nu = 1$, which agrees well with the expected quantized value for a Chern insulator (supported by the quantized R_{xy} and vanishing R_{sym}). The result supports the contact model in Extended Data Fig. 1a and the validity of the calibration procedure of the contact resistance. The quantized R_{xy} and R_{2t} at $\nu = 1$, in accordance with the Landauer–Büttiker formalism with transparent contacts, also support that the junctions between heavily doped and lightly doped $tMoTe_2$ are nearly transparent[8,10,52]. Extended Data Fig. 1d shows the temperature dependence of the calibrated contact resistance (for one contact). The weak temperature dependence indicates that the contacts are in the tunnel contact limit. The contact design here involving a tunnel barrier yields a contact resistance that is smaller than the reported values in earlier studies of $tMoTe_2$ (about 100 kΩ)[25,26].

Landauer–Büttiker analysis of ballistic edge transport

The low-temperature ballistic edge transport can be modelled using the Landauer–Büttiker analysis. Unlike the chiral edge states, the helical edge states can be equilibrated at the electrical contact and are therefore populated according to the chemical potential of the contact from which they emanate[8,10]. This leads to the equivalent circuits in Fig. 3a with a quantized resistance of $2h/(\nu e^2)$ per edge (that is, between two adjacent contacts) for the QSH insulators at $\nu = 2, 3, 4$ and 6. Note that the edge between two shorted electrodes, which share the same chemical potential, does not contribute any resistance. We can compute the two-terminal channel resistance, $R_{2t} = \frac{1}{\nu}, \frac{4}{3\nu}, \frac{3}{2\nu}, \frac{2}{\nu}$ (in units of h/e^2), for the measurement configurations from left to right in Fig. 3a. By contrast, R_{2t} for the $\nu = 1$ Chern insulator with a chiral edge state is expected to be independent of the measurement configuration if no equilibration with the contacts occurs. Figure 3b–e and Extended Data Fig. 4 show good agreement between our experiment and the above analysis.

Similarly, we can compute the four-terminal nonlocal resistance R_{NL} with the measurement configuration shown in Fig. 1f (inset) for the QSH insulators. The nonlocal resistance is determined by $R_{NL} = V_{NL}/I$, where I is the total two-terminal bias current and V_{NL} is the voltage drop at one edge. We obtain $R_{NL} = \frac{1}{2\nu}\frac{h}{e^2}$ for $\nu = 2, 3, 4$ and 6 (dashed lines in Fig. 1c). The experimental result is in good agreement with the quantized value at $\nu = 2$, 10–20% smaller at $\nu = 3$ and 4, and substantially smaller at $\nu = 6$. The discrepancies are probably caused by bulk

conduction, particularly for the smaller gap states at higher filling factors. (Note that R_{NL} is exponentially suppressed[54] for the bulk-dominate transport for $E > E_c$.) Using the same circuit model, we can obtain $R_{sym} = 0$ for the QSH insulators in the measurement configuration of Fig. 1d, which is effectively a bridge circuit for the helical edge resistors. Again, the results (Fig. 1c) are in good agreement with the Landauer–Büttiker analysis.

Data availability

Source data are provided with this paper. All other data are available from the corresponding authors upon reasonable request.

49. Wang, L. et al. One-dimensional electrical contact to a two-dimensional material. *Science* **342**, 614–617 (2013).
50. Lau, C. N., Bockrath, M. W., Mak, K. F. & Zhang, F. Reproducibility in the fabrication and physics of moiré materials. *Nature* **602**, 41–50 (2022).
51. Xia, Z. et al. Optical readout of the chemical potential of two-dimensional electrons. *Nat. Photon.* 10.1038/s41566-024-01377-3 (2024).
52. Büttiker, M. Absence of backscattering in the quantum Hall effect in multiprobe conductors. *Phys. Rev. B* **38**, 9375–9389 (1988).
53. Pack, J. et al. Charge-transfer contact to a high-mobility monolayer semiconductor. Preprint at arxiv.org/abs/2310.19782 (2023).
54. Abanin, D. A. et al. Giant nonlocality near the Dirac point in graphene. *Science* **332**, 328–330 (2011).

Acknowledgements We thank C. Jian, A. H. MacDonald, C. Kane, L. Fu, A. Bernevig, N. Regnault, J. Yu, T. Devakul, A. Reddy and E.-A. Kim for their discussions. This work was primarily supported by the US Department of Energy, Office of Science, Basic Energy Sciences, under award no. DE-SC0019481. It was also funded in part by the Air Force Office of Scientific Research under award no. FA9550-20-1-0219, the Cornell University Materials Research Science and Engineering Center DMR-1719875 and the Gordon and Betty Moore Foundation (grant no. GBMF11563; https://doi.org/10.37807/GBMF11563) for device fabrication and thermodynamic measurements. We used the Cornell NanoScale Facility, an NNCI member supported by NSF Grant NNCI-2025233, for sample fabrication. The growth of the hBN crystals was supported by the Elemental Strategy Initiative of MEXT, Japan, and CREST (JPMJCR15F3), JST. K.F.M. acknowledges support from the David and Lucille Packard Fellowship.

Author contributions K.K., B.S. and Y.Q. fabricated the devices, performed the transport measurements and analysed the data. Y.Z. and Z.X. performed the thermodynamic measurements. K.W. and T.T. grew the bulk hBN crystals. K.K., K.F.M. and J.S. designed the scientific objectives and oversaw the project. All authors discussed the results and commented on the paper.

Competing interests The authors declare no competing interests.

Additional information

Supplementary information The online version contains supplementary material available at https://doi.org/10.1038/s41586-024-07214-5.

Correspondence and requests for materials should be addressed to Kaifei Kang, Jie Shan or Kin Fai Mak.

Peer review information *Nature* thanks Masataka Mogi and the other, anonymous, reviewer(s) for their contribution to the peer review of this work. Peer reviewer reports are available.

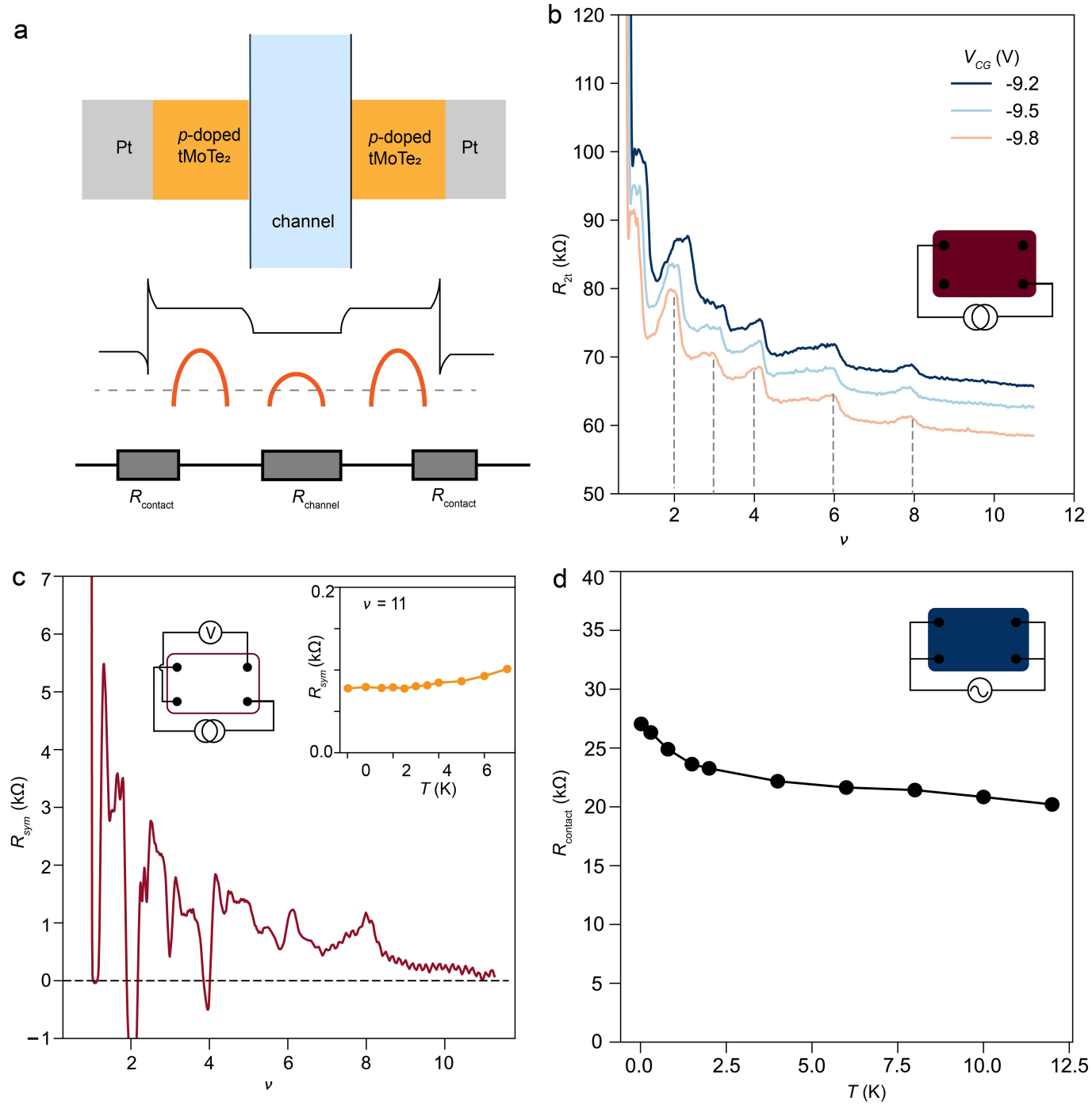

Extended Data Fig. 1 | Contact resistance characterization. a, Top: schematic of the device contact and channel. The Pt electrodes (grey) are contacted to the $tMoTe_2$ channel (blue) through heavily hole-doped $tMoTe_2$ contact regions (orange). Middle: schematic valence band alignment of the $tMoTe_2$ contact and channel regions (solid red lines). Dashed line: Fermi level; solid black line: spatial variation of the work function. Tunnel barriers are at the Pt junctions, but the heavily-to-lightly doped $tMoTe_2$ junctions are transparent. Bottom: equivalent circuit model for two-terminal measurements with $R_{channel}$ and $R_{contact}$ denoting the channel resistance and the contact resistance at the Pt junction, respectively. **b**, Filling factor dependence of two-terminal resistance R_{2t} at different contact gate voltages ($E \approx 0$, T=20 mK and $B_\perp$=0.1 T). Inset: measurement configuration. R_{2t} at the highest fillings is approximately the sum of resistances in series for two contacts. **c**, Filling factor dependence of four-terminal resistance R_{sym} measured with the configuration in the left inset. The resistance drops to about 100 Ω at $\nu = 11$, which is nearly temperature independent (right inset). **d**, Temperature dependence of contact resistance (for one contact) calibrated for the two-terminal configuration in the inset.

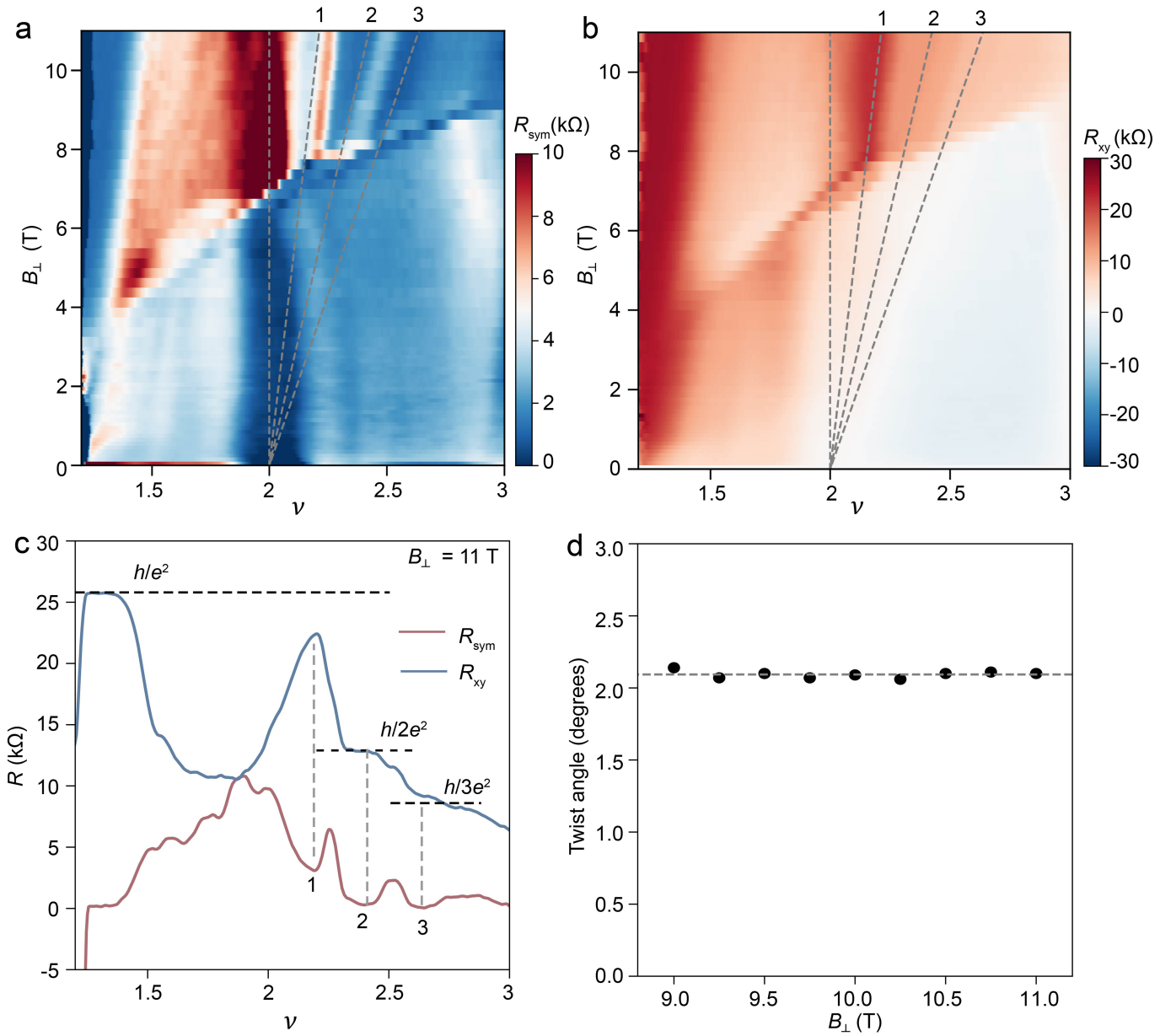

Extended Data Fig. 2 | Twist angle calibration. a,**b**, Four-terminal resistance R_{sym} (**a**) and Hall resistance R_{xy} (**b**) versus out-of-plane magnetic field $B_\perp$ and filling factor ν at $E = 0.06$ V/nm and 20 mK. The measurement configuration is shown in the inset of Fig. 1d. Dashed lines denote Landau level $\nu_{LL} = 1$, 2 and 3 emerging from $\nu = 2$ above $B_\perp \approx 7$-8 T. The dispersing state at low filling factors is the $\nu = 1$ Chern insulator. **c**, Line cut of **a**,**b** at $B_\perp = 11$ T. The vertical dashed lines mark Landau level $\nu_{LL} = 1$, 2 and 3 with nearly quantized R_{xy} and R_{sym} minimum; the horizontal dashed lines denote the expected quantized value of $R_{xy} = \frac{h}{\nu_{LL}e^2}$. **d**, Twist angle calibrated from Landau level spacing at $B_\perp$ ranging from 9 T to 11 T. No field dependence is observed. The mean of the twist angle is 2.10 degrees (dashed line) and the uncertainty is about ±0.05 degrees.

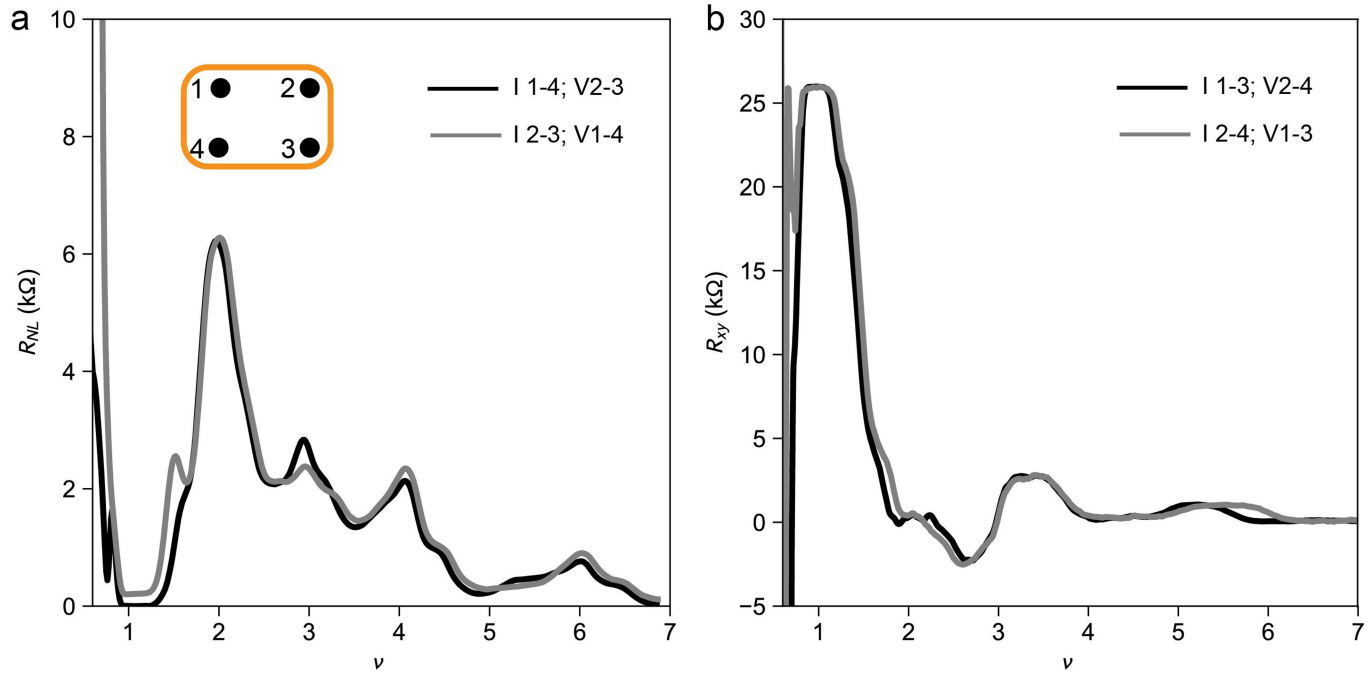

Extended Data Fig. 3 | Symmetric device channel. a,**b**, Filling factor dependence of four-terminal nonlocal resistance R_{NL} (**a**, $B_\perp$=0.1 T) and Hall resistance R_{xy} (**b**, $B_\perp$=0.2 T) at E≈0 and T = 20 mK. The inset shows the device channel with contact 1–4. I: current bias; V: voltage probe. The two curves in each panel correspond to swapped source-drain and voltage probe pairs. The nearly identical results demonstrate a highly symmetric two-dimensional channel.

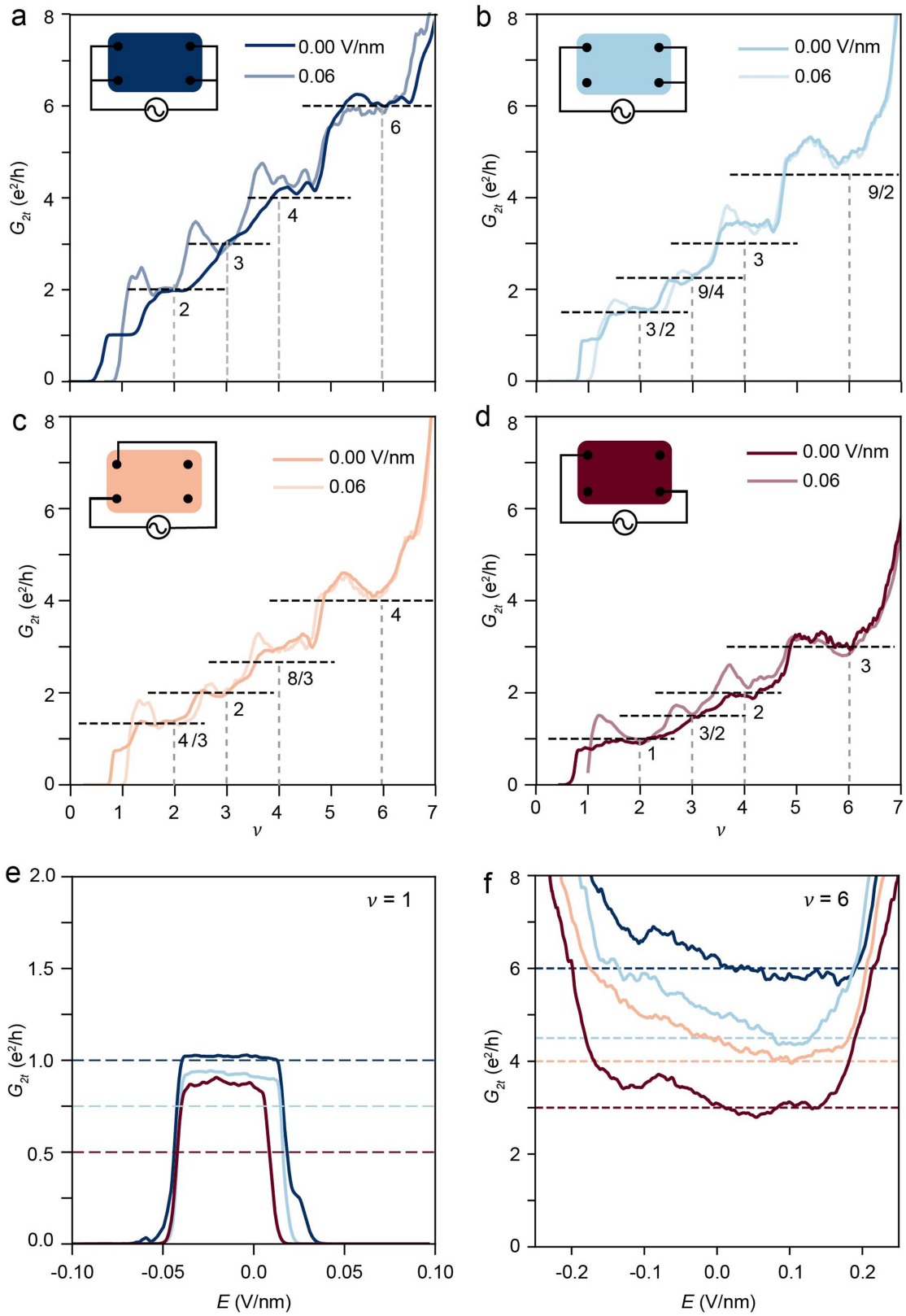

Extended Data Fig. 4 | Additional nonlocal two-terminal transport data. **a**-**d**, Filling factor dependence of two-terminal conductance G_{2t} (in units of $\frac{e^2}{h}$) at two electric fields inside the layer-hybridized regime. Inset: measurement configuration. The dashed lines denote the expected quantized values of G_{2t} at $\nu = 2, 3, 4$ and 6. **e**,**f**, Electric-field dependence of G_{2t} (in units of $\frac{e^2}{h}$) at $\nu = 1$ (**e**) and $\nu = 6$ (**f**) at 20 mK. The horizontal dashed lines denote the expected conductance ν, $\frac{3}{4}\nu$, $\frac{2}{3}\nu$ and $\frac{1}{2}\nu$ in descending order. The colour of the lines matches the colour of the channels in **a**–**d**. Magnetic field 0.3 T is applied to fully polarize the $\nu = 1$ Chern insulator.

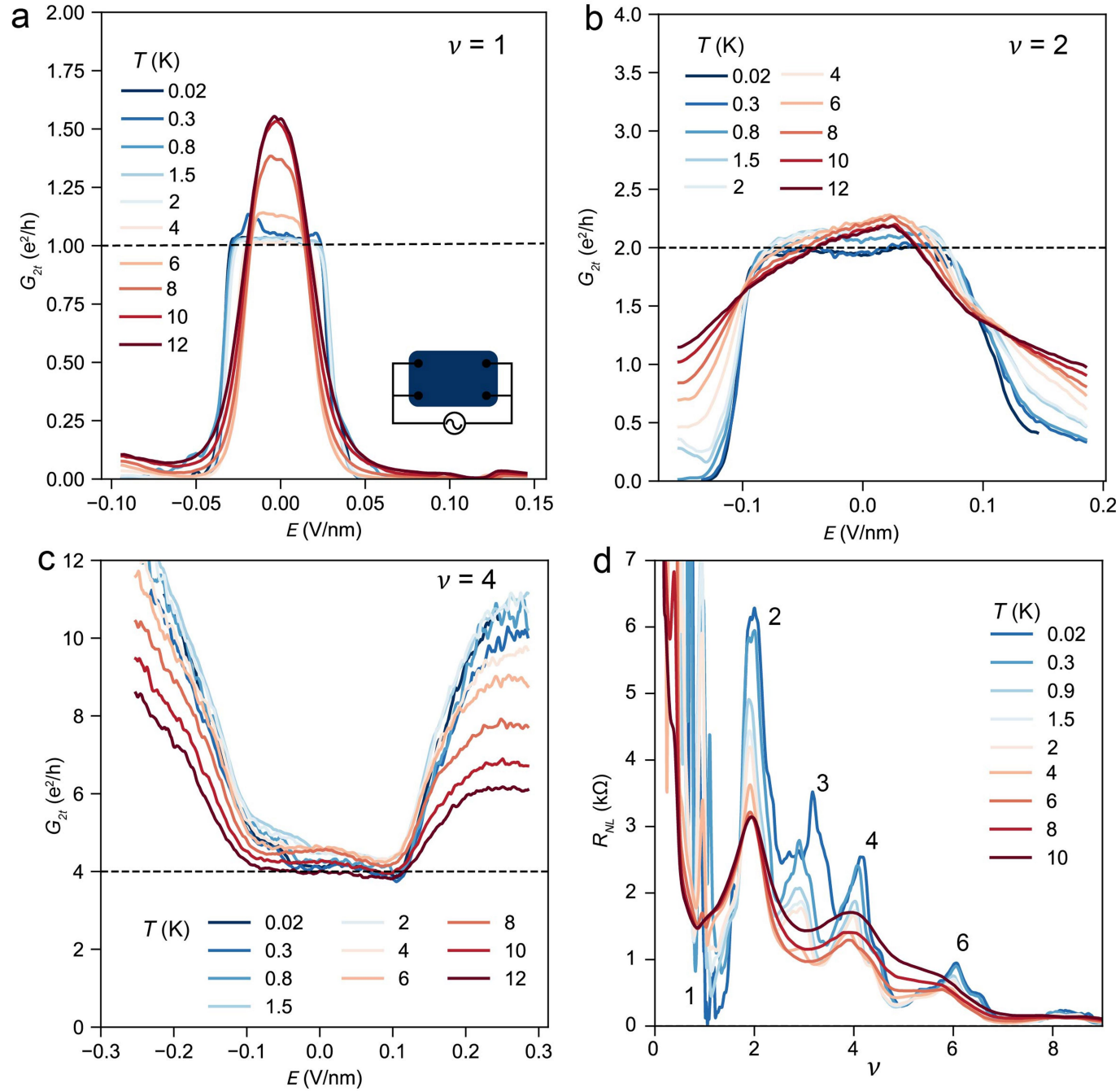

Extended Data Fig. 5 | Additional temperature dependence data. **a**–**c**, Electric-field dependence of two-terminal conductance, G_{2t} (in units of $\frac{e^2}{h}$), at varying temperatures for $\nu = 1$ (**a**), $\nu = 2$ (**b**) and $\nu = 4$ (**c**). The horizontal dashed lines denote the quantized value $G_{2t} = \frac{\nu e^2}{h}$. The measurement configuration is shown in the inset of **a**. **d**, Filling factor dependence of four-terminal nonlocal resistance R_{NL} at $E \approx 0$ and varying temperatures. R_{NL} at $\nu = 2, 3, 4$ and 6 decreases with increasing temperature as bulk conduction becomes more important.

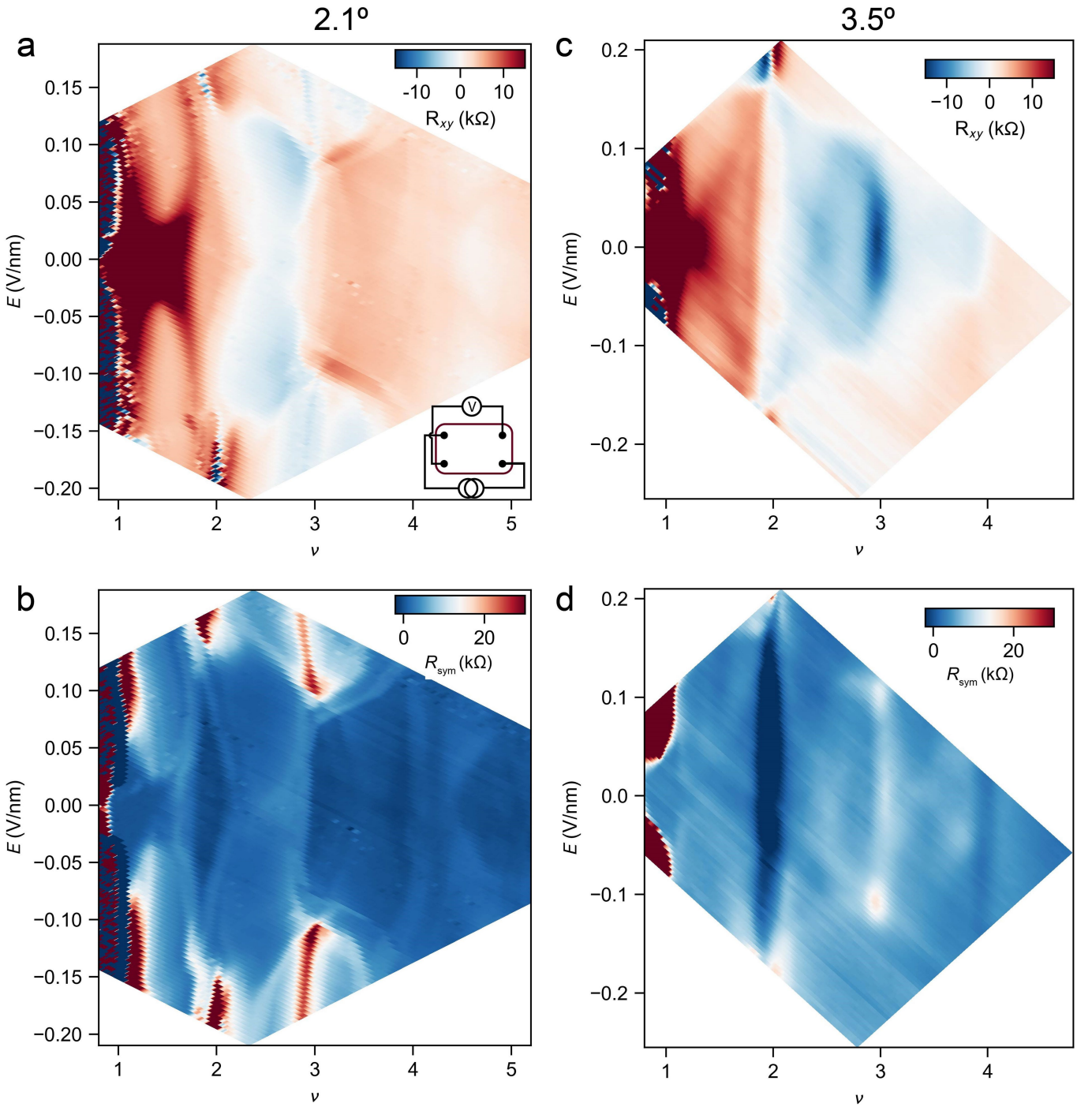

Extended Data Fig. 6 | Twist angle effects. a,**b**, Four-terminal Hall resistance R_{xy} (**a**) and R_{sym} (**b**) versus out-of-plane electric field and filling factor for 2.1-degree $tMoTe_2$ device at $B_\perp = 5$ T and 20 mK. The measurement configuration is shown in the inset of **a**. Both R_{sym} and R_{xy} are small near $\nu = 3$ in the layer-hybridized regime even under high magnetic fields. **c**,**d**, Same as **a**,**b** for 3.5-degree $tMoTe_2$ device at $B_\perp = 4$ T and 1.6 K. A large negative R_{xy} is accompanied by a weak R_{sym} dip near $\nu = 3$ in the layer-hybridized regime (even though at higher temperature and lower magnetic field). The large Hall response suggests a valley-polarized state (rather than a fractional QSH insulator) at $\nu = 3$.

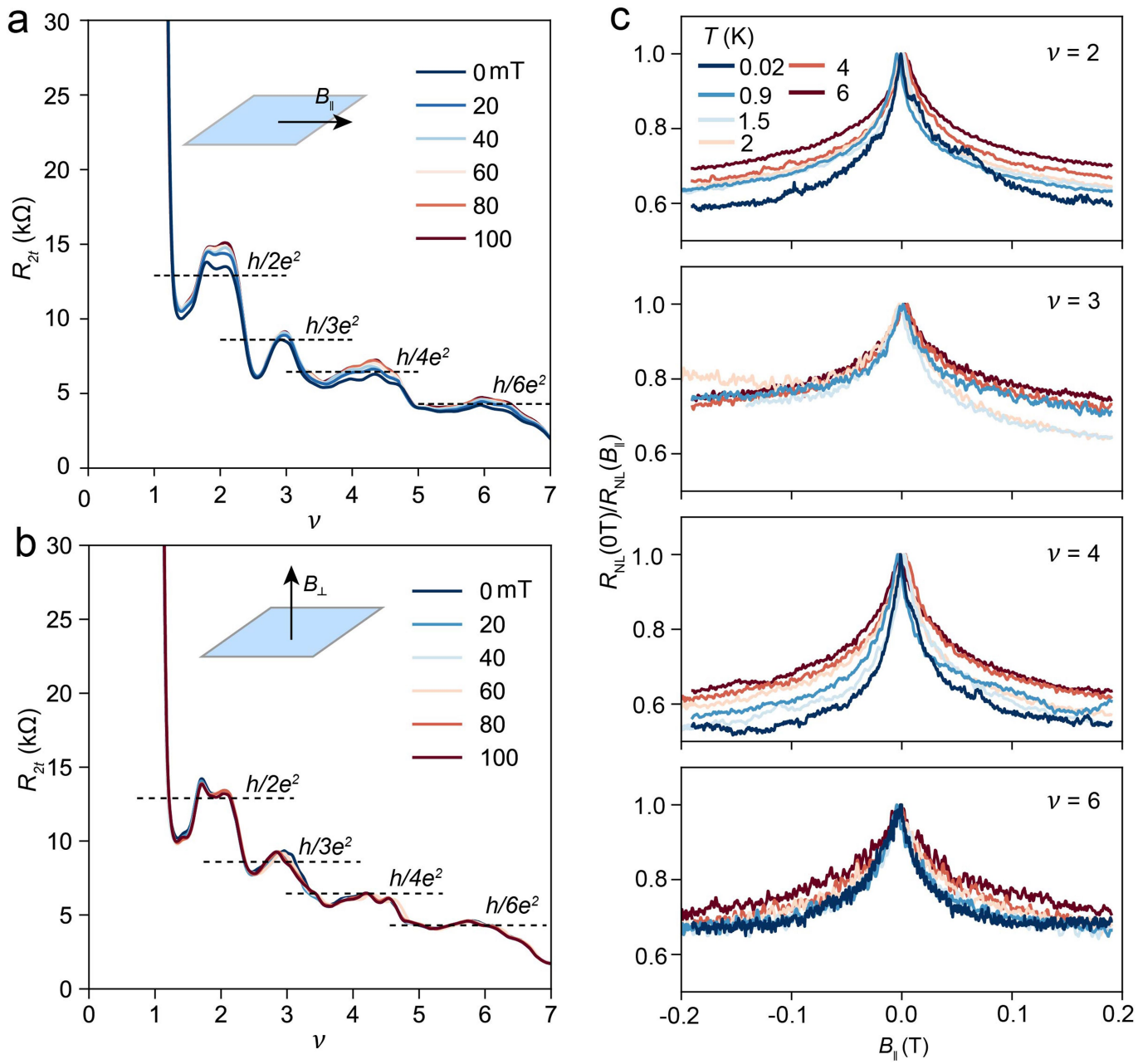

Extended Data Fig. 7 | Anisotropic magneto-response. a,**b**, Filling factor dependence of two-terminal resistance R_{2t} at varying in-plane (**a**) and out-of-plane (**b**) magnetic fields ($E = 0.06$ V/nm and $T = 20$ mK). Whereas R_{2t} is nearly independent of $B_\perp$, it increases with $B_\parallel$. The horizontal dashed lines denote the quantized value $R_{2t} = \frac{h}{2}$ at $\nu = 2, 3, 4$ and 6. **c**, In-plane magnetic field dependence of $\frac{R_{NL}(B_\parallel = 0T)}{R_{NL}(B_\parallel)}\frac{\nu e^2}{}$ at varying temperatures for $\nu = 2, 3, 4$ and 6, where R_{NL} is the nonlocal four-terminal resistance. At all filling factors the cusp at zero magnetic field is broadened as temperature increases. The anisotropic magneto-response supports that the helical edge states carry Ising spins. Because of spin-S_z conservation, the edge states are immune to $B_\perp$, but are susceptible to gap opening and spin mixing under $B_\parallel$, thus increasing R_{2t} and R_{NL}. The anisotropic magneto-response also contrasts with the expected bulk-dominant transport, which would show exactly the opposite magnetic field dependence, namely, strong out-of-plane but negligible in-plane magnetic field dependence.

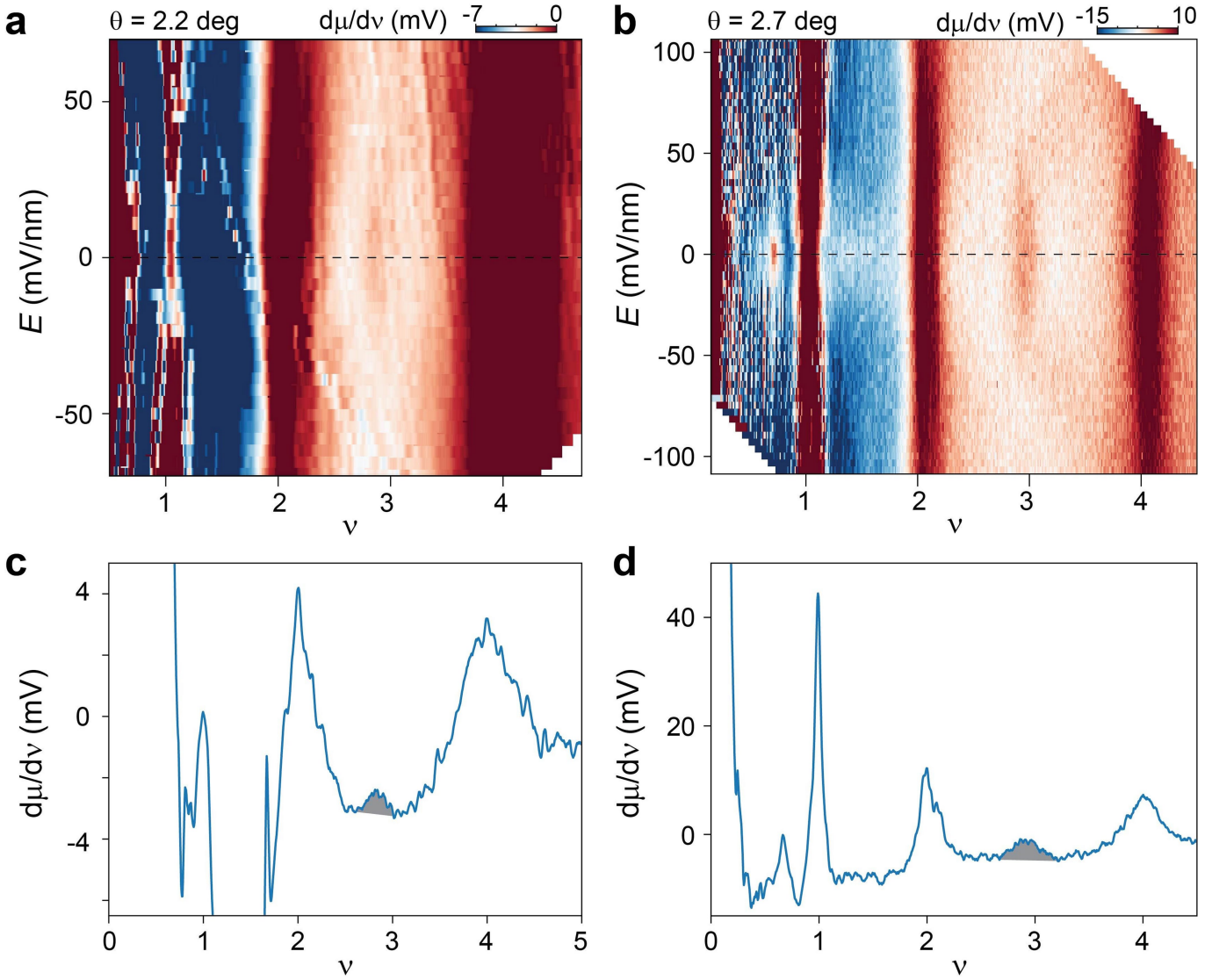

Extended Data Fig. 8 | Incompressibility measurements on 2.2- and 2.7-degree $tMoTe_2$. **a**,**b**, Electronic incompressibility for 2.2-degree (**a**) and 2.7-degree (**b**) $tMoTe_2$ versus vertical electric field E and filling factor ν at 1.6 K ($B_\perp = 0$ T). In addition to the incompressible states at $\nu = 1$, 2 and 4, a weak incompressible state is observed at $\nu = 3$ in the small electric field, layer-hybridized region. **c**,**d**, The corresponding filling factor dependence of the electronic incompressibility at $E = 0$ V/nm (along the dashed lines in **a** and **b**). The grey-shaded area provides an estimate of the charge gap size at $\nu = 3$ (about 0.12 meV and 0.8 meV for 2.2- and 2.7-degree sample, respectively). Note that the true gap size is higher because of the relatively higher base temperature (1.6 K) for the compressibility measurements.